

# Articles

## Improvement in Plume Dispersion Formulas for Stack Emissions Using Ground-based Imaging-DOAS Data

Hanlim Lee, Jaeyong Ryu,<sup>†</sup> Ukkyo Jeong,<sup>‡</sup> Youngmin Noh,<sup>§</sup> Sung Kyun Shin,<sup>§</sup> Hyunkee Hong, and Soonchul Kwon<sup>#,a,\*</sup>

*Department of Spatial Information Engineering, Pukyong National University, Busan 608-737, Korea*

*<sup>†</sup>Department of Urban Environmental Engineering, Kyungnam University, Changwon 631-701, Korea*

*<sup>‡</sup>Department of Atmospheric Sciences, Yonsei University, Seoul 120-749, Korea*

*<sup>§</sup>School of Environmental Science and Engineering, Gwangju Institute of Science and Technology, Gwangju 500-712, Korea*

*<sup>#</sup>School of Civil and Environmental Engineering, Georgia Institute of Technology, GA 30332, USA*

*\*E-mail: lksch76@gmail.com*

*Received July 14, 2014, Accepted August 1, 2014*

This study introduces a new method of combining Imaging Differential Optical Absorption Spectroscopy (Imaging-DOAS) data and plume dispersion formulas for power plant emissions to determine the three-dimensional structure of a dispersing pollution plume and the spatial distributions of trace gas volume mixing ratios (VMRs) under conditions of negligible water droplet and aerosol effects on radiative transfer within the plume. This novel remote-sensing method, applied to a power plant stack plume, was used to calculate the two-dimensional distributions of sulfur dioxide (SO<sub>2</sub>) and nitrogen dioxide (NO<sub>2</sub>) VMRs in stack emissions for the first time. High SO<sub>2</sub> VMRs were observed only near the emission source, whereas high NO<sub>2</sub> VMRs were observed at locations several hundreds of meters away from the initial emission. The results of this study demonstrate the capability of this new method as a tool for estimating plume dimensions and trace gas VMRs in power plant emissions.

**Key Words :** Plume dispersion, Mixing ratio, DOAS, Sulfur dioxide, Nitrogen dioxide

### Introduction

Sulfur dioxide (SO<sub>2</sub>) and nitrogen dioxide (NO<sub>2</sub>) are short-lived atmospheric pollutants emitted from a variety of sources, and play leading roles in regional and global atmospheric chemistry. The main global anthropogenic SO<sub>2</sub> sources are related to energy production such as fossil fuel combustion processes in power plants. High-temperature fossil-fuel combustion is also known to generate nitrogen oxides (NO<sub>x</sub> = NO + NO<sub>2</sub>); this process accounts for approximately 20–25 Tg<sub>N</sub> yr<sup>-1</sup> of the global NO<sub>x</sub> emission budget. Understanding and reducing NO<sub>x</sub> emissions is an important environmental goal because high levels of NO<sub>x</sub> are known to be detrimental to vegetation and to human health.<sup>1-4</sup>

In an attempt to assess the sources of atmospheric pollutants, researchers have monitored trace gases emitted from various types of point sources, such as power plant stacks and volcanoes. To aid in the understanding of the temporal and spatial characteristics of trace gases emitted and dispersed in pollution plumes, extensive research has been conducted to develop several types of remote sensing techniques, including COrrrelation SPEctrometer (COSPEC), Fourier-Trans-

form spectroscopy in the IR (FTIR), and Differential Optical Absorption Spectroscopy (DOAS).<sup>5-8</sup>

Among these recently developed remote sensing techniques, passive DOAS measurements have been widely employed to investigate the spatial distributions of trace gases in both volcanic plumes and power plant emissions.<sup>9-16</sup> Passive DOAS directly measures the slant column density (SCD) of an absorber (*e.g.*, SO<sub>2</sub>), which is the integral of the absorber concentration over the path between a light source and the detector. The SCDs of different absorbers can be obtained over a large area in scanned slices, which allows measurements of the spatial distributions of trace gases in plumes. Values of the SCD, however, can be increased not only by increasing the concentration (or volume mixing ratio, VMR) of a species, but also by a longer absorption path length, as a longer path length leads to an absolute increase in the measured absorbance. The use of the VMR as a measure is prevalent in both environmental assessments of pollution emitters and in the regulation of pollutant levels. Thus, there exists a need for the conversion of SCD data for trace gases to VMR-equivalent data.

As part of an effort to convert SCD data in pollution plumes to VMR data, previous studies<sup>9,17</sup> have attempted to convert SCD measured by Imaging-DOAS into VMRs using absorption light path length information obtained from

<sup>a</sup>Present address: Samsung Advanced Institute of Technology, Samsung Electronics Co., Ltd, Samsung-ro, Gyeonggi-do 443-803, Korea

simple assumption of a circular cross section of the plume. However, large uncertainties in the assumed absorption light path lengths can cause large errors in the SCD to VMR conversion. In the present study, we present a novel technique for this conversion: the SO<sub>2</sub> and NO<sub>2</sub> SCD distributions measured in a power plant plume by passive Imaging-DOAS are used to modify known plume dispersion formulas relevant to coastal wind conditions at the measurement site. Specifically, the three-dimensional (3D) chemical composition of a pollution plume emitted from a power plant stack is first estimated using both Imaging-DOAS data and modeled plume dispersion equations. This estimated 3D calculation of trace gas concentrations within the plume is then applied to SCD data to obtain the spatial distributions of geometrical absorption light path lengths at each Imaging-DOAS measurement pixel. Having estimated both SCD and absorption light path lengths, the VMRs are then calculated; from this calculation, we present, for the first time, the two-dimensional (2D) distributions of SO<sub>2</sub> and NO<sub>2</sub> mixing ratios within the pollution plume at different distances from the initial emission.

### Data and Analysis

**2D Distributions of SO<sub>2</sub> and NO<sub>2</sub>.** The Imaging-DOAS technique is an absorption spectrometer that utilizes scattered sunlight as a light source and measures the attenuation of solar radiation, through a column of the atmosphere, across a broad range of wavelengths. From these data, the 2D spatial

distributions of trace gases with known absorptions, such as SO<sub>2</sub> and NO<sub>2</sub>, can be measured.<sup>9</sup> The 2D distributions of SO<sub>2</sub> and NO<sub>2</sub>, which were simultaneously obtained from Imaging-DOAS measurements in a previous study, are shown in the previous study.<sup>18</sup> In the present study, the 2D distributions of SO<sub>2</sub> and NO<sub>2</sub> are used for the conversion of signal into VMR. The instrument, field measurement conditions, and spectral analysis for obtaining the 2D distributions of SO<sub>2</sub> and NO<sub>2</sub> are described in detail elsewhere<sup>18</sup> and will be summarized briefly here.

The Imaging-DOAS data were obtained from measurements that took place near the TaeAn power plant stacks at a remote site located off the west coast of Korea (36.54°N, 126.14°E) on 17 October 2008. Solar radiance measurements, as captured through plumes emanating from the power plant stacks, were obtained and the recorded radiance data were analyzed to obtain SO<sub>2</sub> and NO<sub>2</sub> SCDs using the WinDOAS software<sup>19</sup> and the DOAS method.<sup>20</sup> To retrieve the SO<sub>2</sub> and NO<sub>2</sub> SCDs, both species were simultaneously fitted to their obtained optical densities from the logarithm of each Fraunhofer reference spectra (FRS), divided by the respective spectrum over the wavelength interval containing the SO<sub>2</sub> and NO<sub>2</sub> absorption bands.

**Optimal Estimation of Plume Dimensions and Light Path Lengths within the Invisible Plume.** Figure 1 presents a procedure diagram for estimating the 3D structure of the plume and the lengths of light paths. This method was applied to calculate the VMRs of trace gases for each pixel (14.3 m (h) × 3.9 m (v)) in the plume. Initially, measured and

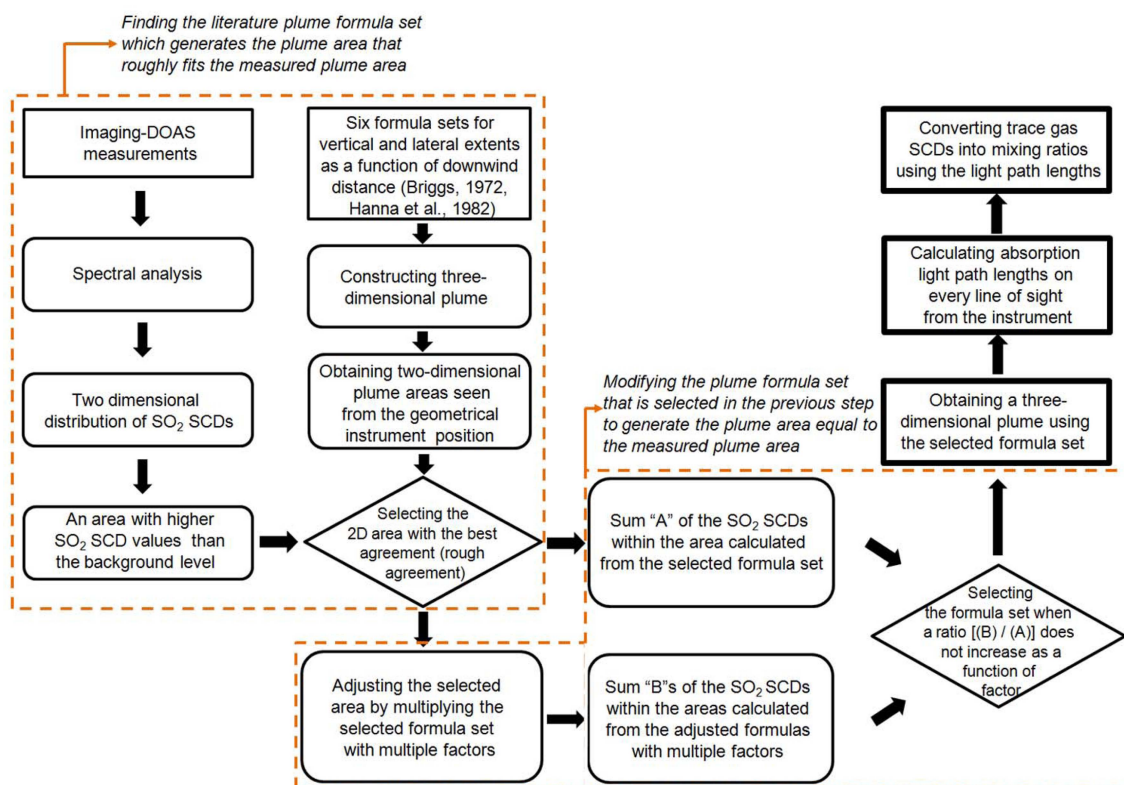


**Figure 1.** The procedure for calculating plume dimensions and light path lengths using Imaging-DOAS. Plume formulas are obtained from Table 1.

**Table 1.** Formulas for lateral and vertical dispersion coefficients,  $\sigma_y(x)$  and  $\sigma_z(x)$ , as a function of downwind distance,  $x$ (m), for rural conditions over land.<sup>21,22</sup> In Pasquill stability class definitions, A and F indicate the most unstable and stable atmospheric conditions, respectively

Pasquill stability classes	$\sigma_y$ , m	$\sigma_z$ , m
A	$0.22x(1 + 0.0001x)^{-1/2}$	$0.20x$
B	$0.16x(1 + 0.0001x)^{-1/2}$	$0.12x$
C	$0.11x(1 + 0.0001x)^{-1/2}$	$0.08x(1 + 0.0002x)^{-1/2}$
D	$0.08x(1 + 0.0001x)^{-1/2}$	$0.06x(1 + 0.0015x)^{-1/2}$
E	$0.06x(1 + 0.0001x)^{-1/2}$	$0.03x(1 + 0.0003x)^{-1}$
F	$0.04x(1 + 0.0001x)^{-1/2}$	$0.016x(1 + 0.0003x)^{-1}$

simulated plume areas were compared to determine a plume formula that yielded a simulated plume area as same size as the measured plume area. For these comparisons, we used SO<sub>2</sub> SCD data from a previous study<sup>18</sup> to define the fresh plume area as a function of downwind distance, as SO<sub>2</sub> concentrations in fresh plumes are clearly distinguishable from the background SO<sub>2</sub> levels and thus the edges of the pollution cloud are relatively easy to define from measurements. To compare the observed 2D SO<sub>2</sub> area with simulated plume areas, 3D plume concentrations were calculated using six formula sets for pollution dispersion under different atmospheric conditions, as illustrated in Table 1.<sup>21,22</sup> From these calculations, we obtained the lateral dispersion coefficient ( $\sigma_y$ ) and vertical dispersion coefficient ( $\sigma_z$ ) as a function of downwind distance depending on six Pasquill stability classes (A to F; least stable to most stable atmospheric conditions, respectively). Six versions of a 3D plume were constructed using this six-formula set, assuming an elliptical plume shape, and accounting for the dimensions between the lateral and vertical axes. Additionally, as the plume was observed to disperse in a slightly slanted upward direction from the horizontal,<sup>18</sup> an empirical constant was used, a power of 0.5, to the  $x$  term to reflect the shape of plume dispersion for the simulated plume dimensions. The 3D plume equation can thus be expressed as follows:

$$\frac{y^2}{\sigma_y^2} + \frac{(z - \sqrt{x})^2}{\sigma_z^2} = 1 \quad (1)$$

where  $\sigma_y$  and  $\sigma_z$  denote lateral and vertical dispersion coefficients, respectively in Table 1. Six different 3D plumes were then calculated by combining Eq. (1) and the plume dispersion formulas in Table 1. Six different 2D plume areas, as seen from the geometrical instrument location, were then obtained from the 3D plumes. Among the six simulated 2D plume areas, the plume dimensions calculated using Formula A for a Pasquill stability class of ‘extremely unstable’ were the closest to the fresh SO<sub>2</sub> plume area obtained by Imaging-DOAS measurements, although the agreement was imperfect. In particular, the plume dimensions calculated using the selected formula were smaller than those observed by the instrument; thus, we modified the formula by multiplying

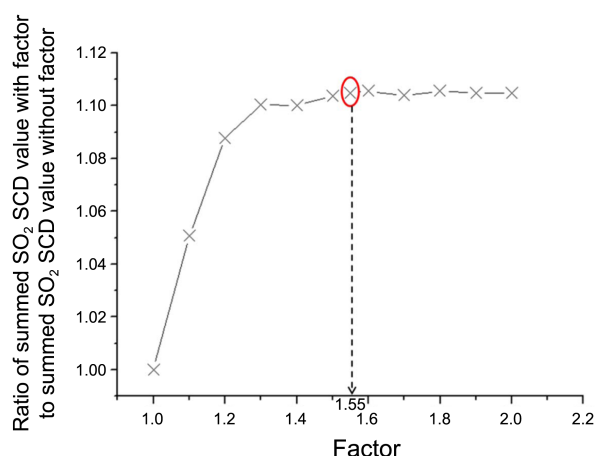


**Figure 2.** The ratio of summed SO<sub>2</sub> SCD plume values calculated with an additional factor to summed SO<sub>2</sub> SCD plume values calculated without any modification as a function of the additional factor value. Highlighted is the best fit factor value.

the selected formula with an empirical constant ranging from 1.0 to 2.0 to obtain the correct plume dimensions.

Figure 2 shows the ratio of the summed SCDs as a function of this new empirical constant, which is the sum of SO<sub>2</sub> SCD values within the calculated plume areas obtained from the modified formula, divided by the sum of SO<sub>2</sub> SCD values within the plume obtained from the unmodified Equation (1). If the ratio increased with an increased value of the empirical factor, the calculated plume area was smaller than the measured plume area. However, if the ratio between modelled and measured SCD values did not increase by increasing the factor value, the calculated plume area was likely as big as or bigger than the measured plume area. Background SO<sub>2</sub> levels were negligible compared with plume SO<sub>2</sub> concentrations; thus, once all of the plume SO<sub>2</sub> SCD was captured, widening the calculated pollution cloud area to include background SO<sub>2</sub> would not significantly increase the calculated SCD. Therefore, the lowest factor value at which the ratio between the calculated and measured SO<sub>2</sub> does not increase by increasing the factor number was the correct value for obtaining the area of a fresh plume with the least background contribution. In this work, it was found that a factor of 1.55 produced the best agreement between the modeled and measured plume areas.

The modified vertical and lateral dispersion coefficients can be rewritten as follows:

$$\sigma_z(x) = 0.31x \quad (2)$$

$$\sigma_y(x) = \frac{0.34x}{\sqrt{1 + 0.0001x}} \quad (3)$$

Figure 3 shows the three-dimensional fresh plume calculated from Eqs. (1), (2), and (3). As calculated by the new plume Eqs. (2) and (3), the lateral and vertical dimensions of the plume at 5 m downwind from the first stack exit were 1.7 and 1.5 m, respectively, compared with the 1.0 and 1.0 m, respectively, obtained from the original plume equations

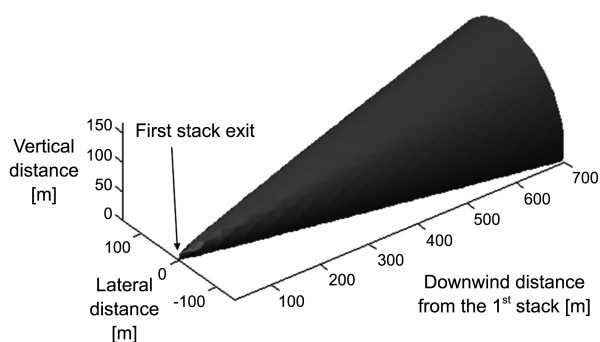


**Figure 3.** Three-dimensional plume obtained from the modified Eqs. (2) and (3) based on the described procedure.

(Table 1). The plume area remained larger with the new equation as the plume dispersed. For example, the lateral and vertical dimensions of the plume at 659 m downwind from the stack exit were 217.8 and 204.5, respectively, m versus 140.5 and 131.9 m, respectively, based on the original plume equation. Full results from these calculations are shown in Table 1.

From these modifications, we then derived a new formula that described the 3D fresh plume by adjusting equations from previous simulations.<sup>18</sup> To calculate the light path length within the plume for each pixel along the instrumental line-of-sight, assuming negligible aerosol and condensed water vapor effects on radiative transfer within the plume, the following equations can be inserted into Eq. (1):

$$y = (y_1 - y_0) \frac{x - x_0}{x_1 - x_0} + y_0 \quad (4)$$

$$z = (z_1 - z_0) \frac{x - x_0}{x_1 - x_0} + z_0 \quad (5)$$

where  $x_0$ ,  $y_0$ , and  $z_0$  are the coordinates of the location of the instrument and  $x_1$ ,  $y_1$ , and  $z_1$  are the coordinates of each pixel of the plume. From these substitutions, Eq. (1) became a polynomial that is a function of  $x$ . Negligible aerosol and condensed water vapor must be assumed as multiple scattering or absorption of light on water droplets and soot particles within the plume can occur and would significantly alter the light path length.

Figure 4 shows the dependence of the absorption light path lengths for each instrument line-of-sight within the

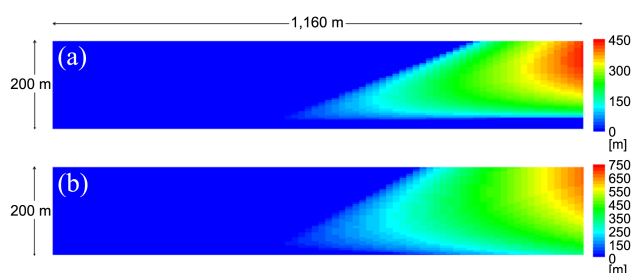


**Figure 4.** Light path lengths within the plume corresponding to each pixel on each instrument line-of-sight. (a) Estimated light path lengths based on Formula A in Table 1. (b) Estimated light path lengths based on Eqs. (2) and (3).

fresh plume. These light path lengths were estimated using Formula A in Table 1 (Figure 4(a)), and using the modified Eqs. (2) and (3) with the fresh plume dimensions shown in Figure 3 (Figure 4(b)). The newly calculated light path lengths increased more quickly with dispersion distance when compared with the path lengths calculated with the old formula (Figure 4(a)). The light path length directly above the stack exit was calculated to be 5.3 m without the equation modifications and 6.2 m with equation modifications. In Figure 4(b), the light path length ranged from 12.8 to 20.6 m for the next plume column, which was 21.7 m downwind from the first stack exit. At the plume column located 355 m downwind distance from the first stack exit, the light path length ranges from 63.4 m at the bottom of the plume to 325.4 m at the plume center in Figure 4(b). The differences in light path lengths between the plume center and the plume edges continued to increase as the plume moved further from the point source and dispersed (Figure 4(b)).

## Results and Discussion

**Spatial Distributions of SO<sub>2</sub> and NO<sub>2</sub> VMRs.** Figure 5 shows the SO<sub>2</sub> (Figure 5(a)) and NO<sub>2</sub> (Figure 5(b)) VMRs over each light path length within the fresh plume, calculated from SO<sub>2</sub> and NO<sub>2</sub> SCDs obtained in a previous study.<sup>18</sup> The SO<sub>2</sub> VMR was very high (17.1 parts per million (ppm)) near the stack exit, and ranged from 10.4 ppm to 29.2 ppm from initial emission to a distance of approximately 50 m downwind. Additionally, the SO<sub>2</sub> VMR was high (>25.0 ppm) for several pixels on the edge of the plume. These high SO<sub>2</sub> VMRs were likely overestimated because of underestimation of the light path length at the plume edge, influenced by the non-linear shape of the plume at the real plume boundary. The SO<sub>2</sub> VMR decreased rapidly with dispersion distance, decreasing to 1 ppm at a distance 150 m downwind from the first stack exit and ranging from 0.0 to 1.1 ppm at the last calculated vertical column located approximately 660 m downwind from the emission point. Examining the vertical distribution revealed that the SO<sub>2</sub> VMRs were higher at the bottom and center of the plume than near the top of the plume.

The spatial distribution of the NO<sub>2</sub> VMR was similar to that of NO<sub>2</sub> SCD shown in the previous study,<sup>18</sup> with high

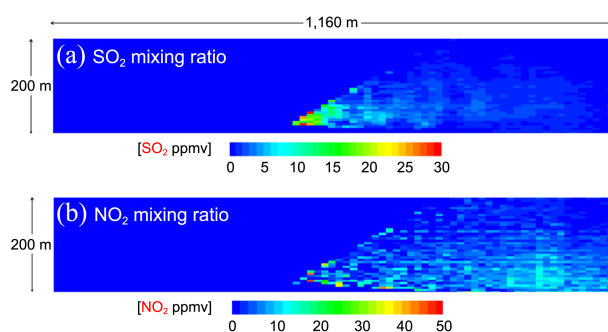


**Figure 5.** Spatial distributions of the SO<sub>2</sub> (a) and NO<sub>2</sub> (b) VMRs obtained from the combined Imaging-DOAS data and plume equations.

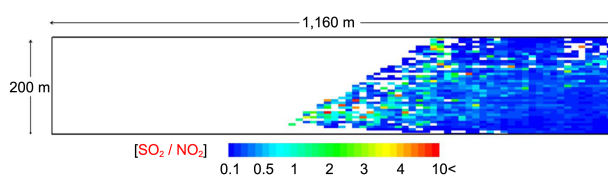


**Figure 6.** The ratio of SO<sub>2</sub> VMR to NO<sub>2</sub> VMR, from the data shown in Figure 5.

NO<sub>2</sub> levels calculated downwind from emission, the opposite of the SO<sub>2</sub> dispersion trend. Similar to the calculated SO<sub>2</sub> plume distribution, areas of high NO<sub>2</sub> were calculated at the edge of the plume (Figure 5(b)). Again, these results suggested that the calculated linear boundary of the estimated plume edge may have caused an underestimation of the light path lengths at the plume edge. With the exception of these abnormally high NO<sub>2</sub> VMRs near the plume edge, the NO<sub>2</sub> VMR ranged from 0.9 to 7.2 ppm within 50 m of emission and increased at downwind distances ranging from 400 to 600 m. It is worthwhile to note that the dilution by background air reduced SO<sub>2</sub> concentration as the plume moved from the emission source, while the oxidation of NO by background oxidants increased the NO<sub>2</sub> concentration, indicating that the plume distribution of NO<sub>x</sub> is significantly dependent on ambient oxidant concentrations in the air.

The SO<sub>2</sub>/NO<sub>x</sub> ratio is a critical parameter in the atmospheric oxidation processes of these gases because SO<sub>2</sub> and NO compete for the same oxidizing radicals, and the oxidation of NO<sub>2</sub> by OH is ten times faster than that of SO<sub>2</sub>.<sup>23</sup> Therefore, we calculated the ratio of SO<sub>2</sub> to NO<sub>2</sub> in the fresh plume emission to reflect the spatial distribution of this competition between SO<sub>2</sub> and NO<sub>x</sub> for oxidants (Figure 6). Any underestimated light path length was eliminated at the plume edges to reduce errors in SO<sub>2</sub> and NO<sub>2</sub> ppm calculations and a low ratio of SO<sub>2</sub> to NO<sub>2</sub> at the plume boundaries was calculated (Figure 5). Slow SO<sub>2</sub> oxidation would cause a high initial ratio of SO<sub>2</sub> to NO<sub>2</sub>, which would suggest that SO<sub>2</sub> was the dominant species in the initial plume and NO was not yet oxidized to NO<sub>2</sub>. Our findings agreed with this: we observed high SO<sub>2</sub> to NO<sub>2</sub> ratios, some greater than 10, near the first stack emission (Figure 6). High SO<sub>2</sub> to NO<sub>2</sub> ratios were also calculated in the area within 300 m downwind of the first stack emission and in the upper part of the plume area where the NO<sub>2</sub> VMRs were lower than those near the ground (Figure 5(b)). The high ratio of SO<sub>2</sub> to NO<sub>2</sub> in those areas could be attributed to lower mixing rates of the plume with background air, which contained high levels of oxidants such as O<sub>3</sub> and OH<sup>-</sup> radicals. In contrast, low ratios of SO<sub>2</sub> to NO<sub>2</sub>, as low as 0.03, were observed at distances 400–600 m downwind from the power plant stack, where a high NO<sub>2</sub> VMR was measured, likely because of the mixture of the plume with oxidant-rich background air.

**Evaluation of Spatial Distributions of SO<sub>2</sub> and NO<sub>2</sub>.** To evaluate the calculated spatial distributions of SO<sub>2</sub> and NO<sub>2</sub>, we compared our calculated data with *in-situ* measurement data, provided by the power plant company (Korea Western Power Co., Ltd). The SO<sub>2</sub> and NO<sub>2</sub> values obtained in this

study were 17.1 ppm and 5.4 ppm, respectively, at the first stack exit whereas those measured by the *in-situ* monitor (EC9850H, ECOTECH, Australia) were 19.2 ppm and 6.3 ppm, respectively. The comparisons were limited to the measurement data at the stack exits because of the difficulty of obtaining access to areas other than the stack exits within the measured plume. Nevertheless, we believed that our monitoring data were similar to the *in-situ* measurement data. The errors of the estimated SO<sub>2</sub> and NO<sub>2</sub> range from 5% to 13% and from 7% to 9%, respectively. These errors were obtained from an error propagation method accounting for spectral fit errors and errors of the estimated absorption path lengths.<sup>24</sup>

## Conclusions

This study introduced a new technique using passive Imaging-DOAS measurements combined with dispersion model formulas to determine the dimensions of and trace gas VMRs in pollution plumes emitted from power plant stacks. We found that the estimated SO<sub>2</sub> and NO<sub>2</sub> VMR distributions differed from their SCD distributions, with high SO<sub>2</sub> VMRs near the stack exit and lower SO<sub>2</sub> VMRs with increased distance from emission. Conversely, high NO<sub>2</sub> VMRs were observed further downwind from the pollution stack. However, high SO<sub>2</sub> and NO<sub>2</sub> VMRs both appeared at the estimated fresh plume edge, which could be attributed to the underestimated lengths of light path through the plume edge where the plume formula cannot closely approximate the true shape of the plume. Further Imaging-DOAS measurements should be taken to fully validate our novel method of calculating trace gas VMRs, covering larger areas and different point emission sources.

**Acknowledgments.** This work was supported by a National Research Foundation of Korea (NRF) grant funded by the Korea government (MEST) (No. 2012R1A1A2004834). The software package WinDOAS used to evaluate the Imaging-DOAS spectra was provided by the Belgium Institute for Space Aeronomy, Belgium.

## References

1. Benkovitz, C. M.; Scholtz, M. T.; Pacyna, J.; Tarrason, L.; Dignon, J.; Voldner, E. C.; Spiro, P. A.; Logan, J. A.; Graedel, T. E. *J. Geophys. Res.* **1996**, *101*(D22), 229-239.
2. Dignon, J. *Atmos. Environ.* **1992**, *26A*, 1157-1163.
3. Holland, E. A.; Dentener, F. J.; Braswell, B. H.; Sulzman, J. M. *Biogeochemistry* **1999**, *46*, 7-43.
4. Agency, U. E. P. *National Air Quality and Emissions Trends Report 1997*, 1998.
5. Sandsten, J.; Edner, H.; Svanberg, S. *Optics Lett.* **1996**, *21*, 1945-1947.
6. *Scanning Infrared Remote Sensing System for Identification, Visualization, and Quantification of Airborne Pollutants, Instrumentation for Air Pollution and Global Atmospheric Monitoring*; Harig, R., Matz, G., Rusch, P., Eds., 2001; Vol. 4574.
7. Love, S. P.; Goff, F.; Schmidt, S. C.; Counce, D.; Pettit, D.; Christenson, B. W.; Siebe, C. *Geophys. Monogr.* **2000**, *116*, 117-138.

8. Verma, S. K.; Deb, M. K.; Verma, D. *Atmos. Res.* **2008**, *90*, 33-40.
  9. Lohberger, F.; Honninger, G.; Platt, U. *Appl. Opt.* **2004**, *43*, 4711-4717.
  10. Bobrowski, N.; Honninger, G.; Galle, B.; Platt, U. *Nature* **2003**, *423*, 273-276.
  11. Bobrowski, N.; Honninger, G.; Lohberger, F.; Platt, U. *J. Volcanol. Geoth. Res.* **2006**, *150*, 329-338.
  12. Bobrowski, N.; von Glasow, R.; Aiuppa, A.; Inguaggiato, S.; Louban, I.; Ibrahim, O. W.; Platt, U. *J. Geophys. Res.* **2007**, *112*, D06311.
  13. Heue, K. P.; Wagner, T.; Broccardo, S. P.; Walter, D.; Piketh, S. J.; Ross, K. E.; Beirle, S.; Platt, U. *Atmos. Chem. Phys.* **2008**, *8*, 6707-6717.
  14. Lee, H.; Kim, Y. J.; Jung, J.; Lee, C.; Heue, K. P.; Platt, U.; Hu, M.; Zhu, T. *J. Environ. Mgt.* **2009**, *90*, 1814-1823.
  15. Louban, I.; Bobrowski, N.; Rouwet, D.; Inguaggiato, S.; Platt, U. *B. Vol.* **2009**, *71*, 753-765.
  16. Pikelnaya, O.; Flynn, J. H.; Tsai, C. *J. Geophys. Res.* **2013**, *118*, 8716-8728.
  17. Lee, H.; Kim, Y. J.; Lee, C. *Environ. Monit. Assess.* **2009**, *152*, 61-70.
  18. Lee, H. L.; Noh, Y. M.; Kwon, S. C.; Hong, H. K.; Han, K. S. *Bull. Korean Chem. Soc.* **2014**, *35*, 1191-1194.
  19. Van Roozendaal, M.; Fayt, C. Uccle, IASB/BIRA, 2001.
  20. Platt, U.; Stutz, S. *Differential Optical Absorption Spectroscopy: Principles and Applications*; Verlag Berlin Heidelberg, 2008.
  21. Briggs, C. A. *Atmos. Environ.* **1972**, *6*, 507-510.
  22. Hanna, S. R.; Briggs, G. A.; P., H. J. R. *Handbook on Atmospheric Diffusion*; Department of Energy, 1982.
  23. Mamane, Y.; Pueschel, R. F. *Atmos. Environ.* **1980**, *14*, 629-639.
  24. Lee, H. L.; Gu, M.; Kim, Y. J.; Hwang, J.; Jung, U. *Atmos. Environ.* **2012**, *54*, 519-528.
-